PCCP

PAPER

View Article Online
View Journal | View Issue

Cite this: *Phys. Chem. Chem. Phys.*, 2015, **17**, 9687

Excited-state intramolecular proton transfer to carbon atoms: nonadiabatic surface-hopping dynamics simulations†

Shu-Hua Xia,[a] Bin-Bin Xie,[a] Qiu Fang,[a] Ganglong Cui*[a] and Walter Thiel*[b]

Excited-state intramolecular proton transfer (ESIPT) between two highly electronegative atoms, for example, oxygen and nitrogen, has been intensely studied experimentally and computationally, whereas there has been much less theoretical work on ESIPT to other atoms such as carbon. We have employed CASSCF, MS-CASPT2, RI-ADC(2), OM2/MRCI, DFT, and TDDFT methods to study the mechanistic photochemistry of 2-phenylphenol, for which such an ESIPT has been observed experimentally. According to static electronic structure calculations, irradiation of 2-phenylphenol populates the bright S_1 state, which has a rather flat potential in the Franck–Condon region (with a shallow enol minimum at the CASSCF level) and may undergo an essentially barrierless ESIPT to the more stable S_1 keto species. There are two S_1/S_0 conical intersections that mediate relaxation to the ground state, one in the enol region and one in the keto region, with the latter one substantially lower in energy. After $S_1 \rightarrow S_0$ internal conversion, the transient keto species can return back to the S_0 enol structure *via* reverse ground-state hydrogen transfer in a facile tautomerization. This mechanistic scenario is verified by OM2/MRCI-based fewest-switches surface-hopping simulations that provide detailed dynamic information. In these trajectories, ESIPT is complete within 118 fs; the corresponding S_1 excited-state lifetime is computed to be 373 fs in vacuum. Most of the trajectories decay to the ground state *via* the S_1/S_0 conical intersection in the keto region (67%), and the remaining ones *via* the enol region (33%). The combination of static electronic structure computations and nonadiabatic dynamics simulations is expected to be generally useful for understanding the mechanistic photophysics and photochemistry of molecules with intramolecular hydrogen bonds.

Received 11th January 2015,
Accepted 10th February 2015

DOI: 10.1039/c5cp00101c

www.rsc.org/pccp

Introduction

Excited-state intramolecular or intermolecular proton transfers are elementary processes occurring in many molecular and biochemical systems[1–5] and electronic devices,[6–9] for example, in natural and artificial photosynthesis,[10,11] water-splitting photocatalysis,[12] green fluorescent proteins,[13,14] and photoswitches.[15] Understanding these excited-state proton transfer processes is important both from fundamental and technological points of view. To this end, numerous computational studies ranging from static electronic structure calculations to nonadiabatic dynamics simulations have been performed in the past few decades.[16–30] Most of these previous studies focused on excited-state proton transfer processes between two highly electronegative atoms, *e.g.* nitrogen, oxygen, and fluorine.[17–20,22,26,27,31–37]

What about excited-state intramolecular proton transfer (ESIPT) in molecules without strong hydrogen bonds, for example, in alcohols or phenols? Such ESIPT processes were first investigated in the 1980s,[38,39] with proton transfer to aromatic carbon atoms being first addressed at the beginning of this century.[40] Since then, Wan and coworkers have systematically explored such excited-state proton transfers in many systems.[41–48] They first studied photochemical deuterium incorporation at the *ortho* and *para* positions of 2-phenylphenol in various solvent mixtures[49] and found that the predominant exchange at the *ortho* position is independent of water and methanol contents, implying an intramolecular process. They also investigated the photochemistry of *o*-hydroxybiaryls, which features not only an efficient excited-state proton transfer to the *ortho* carbon atom of the naphthyl ring, but also a novel ring-closing reaction.[50] Flegel *et al.*[51] studied the photoaddition of water and alcohols to the 9- and 10-positions of the anthracene moiety of 9-(2-hydroxyphenyl)-anthracene in acetonitrile and methanol mixtures and proposed a

[a] *Key Laboratory of Theoretical and Computational Photochemistry, Ministry of Education, College of Chemistry, Beijing Normal University, Beijing 100875, China. E-mail: ganglong.cui@bnu.edu.cn*
[b] *Max-Planck-Institut für Kohlenforschung, 45470 Mülheim an der Ruhr, Germany. E-mail: thiel@mpi-muelheim.mpg.de*

† Electronic supplementary information (ESI) available: Active space in OM2/MRCI computations and Cartesian coordinates of all structures. See DOI: 10.1039/c5cp00101c

mechanism involving water-mediated excited-state proton transfer from the phenolic OH group to the anthracene fragment. Basarić and Wan[52] investigated the potential excited-state proton transfer in four derivatives of 9-(2-hydroxyphenyl)anthracene. Nayak and Wan[53] explored photochemical deuterium incorporation in extended *ortho*-substituted biaryl systems and reported the longest solvent-assisted proton-relay chain. They proposed direct and water-assisted proton transfer mechanisms to explain photohydration at the *ortho* and distal positions, respectively. In these experimental studies, it was generally believed that excited-state intramolecular proton transfer to *ortho* positions is efficient in phenols.

The underlying photophysical and photochemical mechanisms in these systems have not yet been elucidated in detail, *e.g.*, with regard to the relevant structures, proton transfer paths, excited-state potential energy surfaces, lifetimes, and decay channels. We are aware of only one recent theoretical study in this context,[54] which employed the single-reference second-order coupled cluster (RI-CC2) method to explore direct and water-assisted excited-state proton transfer in 2-phenyl-1-naphthol. Given this situation, we decided to perform high-level multi-reference electronic structure computations and trajectory-based surface-hopping dynamics simulations to study the mechanistic photochemistry of the prototypical 2-phenylphenol molecule, with emphasis on the ESIPT process to the *ortho* carbon atom and the deactivation channels leading back to the ground state.

Computational details

Ab initio methods

Ground-state (S_0) conformers were optimized at the B3LYP level.[55–58] The resolution-of-the-identity second-order algebraic diagrammatic construction [RI-ADC(2)] method was employed to optimize excited-state minimum-energy reaction paths.[59–63]

The state-averaged complete active space self-consistent field (SA-CASSCF) method (equal state weights) was used to optimize minima (S_0 and S_1) and minimum-energy conical intersections (S_0/S_1). In all SA-CASSCF geometric optimizations, the active space comprised 10 electrons in 8 orbitals. To obtain more accurate potential energy profiles, single-point MS-CASPT2 calculations[64,65] were performed at the CASSCF optimized geometries. In these MS-CASPT2 calculations, an imaginary shift of 0.2 a.u. was applied to avoid intruder-state issues,[66] and Cholesky decomposition techniques with unbiased auxiliary basis sets were used to evaluate two-electron integrals.[67]

Vertical excitation energies were computed at the TD-CAM-B3LYP[68,69] and MS-CASPT2 levels. The 6-31G* basis set[70,71] was used throughout except for the RI-ADC(2) calculations which employed the def2-SVP basis set.[72] The following codes were used: TDDFT, GAUSSIAN09;[73] DFT and CASSCF optimizations, GAUSSIAN03;[74] MS-CASPT2, MOLCAS7.6;[75] and RI-ADC(2), TURBOMOLE6.5.[76]

OM2/MRCI method

All semiempirical calculations were performed using the OM2/MRCI method as implemented in the MNDO99 code.[77–80] During geometry optimizations, all required energies, gradients, and nonadiabatic coupling elements were computed analytically. Conical intersections were optimized using the Lagrange–Newton approach.[81,82]

In OM2/MRCI calculations, the restricted open-shell HF formalism was applied in the self-consistent field (SCF) treatment (*i.e.*, the orbitals were optimized for the leading configuration of the S_1 state with two singly occupied orbitals). The active space in the MRCI calculations included 12 electrons in 10 orbitals (see ESI†). In terms of the SCF configuration, it comprised the five highest doubly occupied orbitals, two singly occupied orbitals, and the three lowest unoccupied orbitals. For the MRCI treatment, three configuration state functions were chosen as references, namely the SCF configuration and the two closed-shell configurations derived therefrom (*i.e.*, all singlet configurations that can be generated from the HOMO and the LUMO of the closed-shell ground state). The MRCI wavefunction was built by allowing all single and double excitations from these three references.

The nonadiabatic dynamics was studied by performing 1 ps OM2/MRCI trajectory surface-hopping simulations. The initial atomic coordinates and velocities were randomly selected from 5 ps trajectories of ground-state molecular dynamics. The number of excited-state dynamics runs was then chosen according to the computed S_0–S_1 transition probability. A total of 193 surface-hopping trajectories were run, with all relevant energies, gradients, and nonadiabatic coupling vectors being computed on-the-fly as needed. For points with an S_1–S_0 energy gap of less than 10 kcal mol^{-1}, the fewest-switches criterion was applied to decide whether to hop. The time step was chosen to be 0.1 fs for nuclear motion and 0.0005 fs for electronic propagation. The unitary propagator evaluated at a mid-point was used to propagate the electronic motion. The translational and rotational motions were removed in each step. The empirical decoherence correction (0.1 a.u.) proposed by Granucci *et al.* was employed.[83] The final evaluations were done for the 148 trajectories that finished successfully and satisfied our energy continuity criterion (no changes greater than 30 kcal mol^{-1} between any two consecutive MD steps). Further technical details are given in our previous publications.[26–29,84–86]

Results

Ground-state properties and vertical excitation energies

Apart from the most stable ground-state structure of 2-phenylphenol (S0-ENOL), there is also a minimum for the keto tautomer (S0-KETO), see Fig. 1 and Table 1. For each of the two minima, OM2/MRCI and CASSCF yield similar geometries. S0-ENOL is more stable than S0-KETO by 34.7 (33.7) kcal mol^{-1} at the OM2/MRCI (MS-CASPT2) level.

The computed vertical excitation energies for the first excited singlet state (S_1) are collected in Table 2. The OM2/MRCI value of 4.92 eV agrees very well with the results from MS-CASPT2 (4.99 eV) and TD-CAM-B3LYP (4.93 eV). The calculations are consistent with the experimental value of 4.66 eV

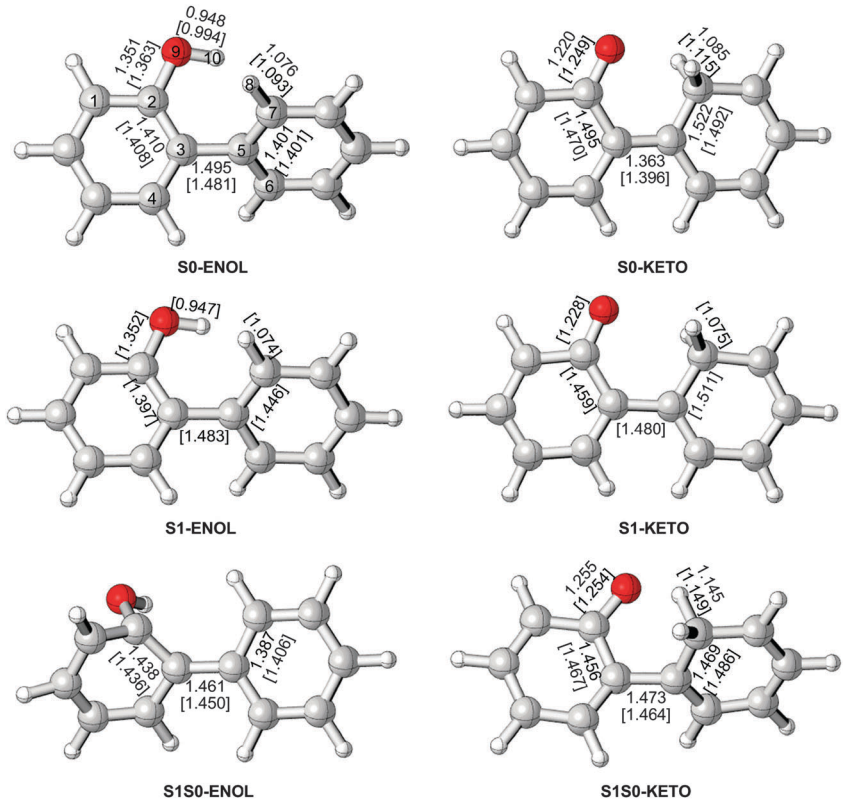

Fig. 1 Stationary points and minimum-energy conical intersections, with selected optimized bond lengths (Å) obtained from OM2/MRCI and CASSCF (in square brackets).

Table 1 Key dihedral angles (degree) of 2-phenylphenol structures from OM2/MRCI and CASSCF optimizations and relative energies ΔE (kcal mol^{-1}) from OM2/MRCI and single-point MS-CASPT2 calculations

Structure	C4C3C2O9	C2C3C5C6	C2C3C5C7	C3C1C2O9	ΔE
OM2/MRCI					
S0-ENOL	179.6	−127.7	52.8	179.7	0.0
S0-KETO	180.0	180.0	0.0	180.0	34.7
S1S0-ENOL	−83.1	154.0	−27.8	140.6	92.1
S1S0-KETO	166.8	−107.9	58.2	−171.7	73.7
CASSCF(10,8)/6-31G*					
S0-ENOL	179.0	−118.1	62.6	179.7	0.0
S0-KETO	−180.0	179.8	−0.2	−180.0	33.7
S1-ENOL	178.2	−132.3	51.2	179.4	103.0
S1-KETO	180.0	180.0	0.0	180.0	74.4
S1S0-ENOL	−96.8	145.9	−35.4	154.8	98.8/100.7
S1S0-KETO	172.4	−113.7	52.8	−174.7	69.8/73.9

Table 2 Computed vertical excitation energies to the first excited singlet state of 2-phenylphenol and the experimental band maximum from laser flash photolysis in solution[49]

	OM2/MRCI	MS-CASPT2	TD-CAM-B3LYP	Exp.
kcal mol^{-1}	113.5	115.0	113.8	107.5
eV	4.92	4.99	4.93	4.66

obtained from laser flash photolysis of 2-phenylphenol in solutions.[49] A slightly lower experimental value of 4.28 eV has been reported for 2-phenyl-1-naphthol featuring more extensive conjugation.[54] The S_1 state at the Franck–Condon point is spectroscopically bright; its oscillator strength is computed to be 0.155 at the TD-CAM-B3LYP level. Molecular orbital analysis shows that the S_0–S_1 electronic transition mainly originates from the HOMO–LUMO single excitation (Fig. 2). The HOMO is mainly localized in the phenolic part, whereas the LUMO is localized in the phenyl group. Hence, the S_1 state is of charge-transfer character, which sets the stage for the subsequent excited-state proton transfer. In fact, this kind of electronic structure change has been found in many similar intramolecularly hydrogen-bonded systems.[18,20,22,26,27,30]

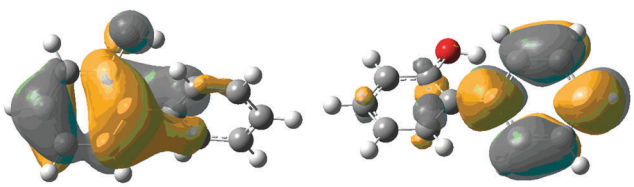

Fig. 2 CAM-B3LYP/6-31G* computed HOMO and LUMO of S0-ENOL responsible for the $S_0 \rightarrow S_1$ vertical excitation.

Excited-state minima

At the CASSCF level, there is a shallow S_1 minimum in the Franck–Condon region of 2-phenylphenol (S1-ENOL), which is computed to lie 103.0 kcal mol^{-1} above the S0-ENOL minimum in single-point MS-CASPT2 calculations. At the OM2/MRCI

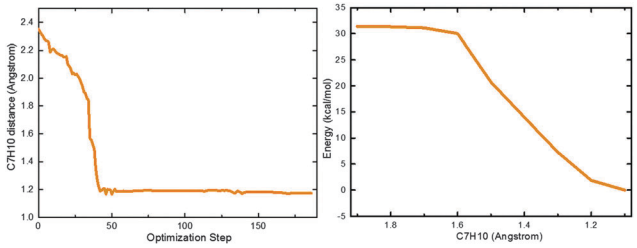

Fig. 3 (left) OM2/MRCI optimization path starting from the enol minimum, which leads directly to a keto species after about 50 steps; (right) RI-ADC(2)/def2-SVP computed minimum-energy reaction path with respect to the C7–H10 proton transfer reaction coordinate. See text for discussion.

level, no such S_1 minimum could be located since all minimizations starting from the S0-ENOL equilibrium geometry led directly to the S_1 keto species (S1-KETO), see the left panel of Fig. 3. Likewise, the minimum-energy path for proton transfer computed at the RI-ADC(2)/def2-SVP level indicates an essentially barrierless excited-state enol–keto tautomerization, see the right panel of Fig. 3. This is also verified by OM2/MRCI nonadiabatic dynamics simulations (*vide infra*).

CASSCF optimization yields another S_1 minimum in the keto region (S1-KETO, see Fig. 1). At this geometry, there is no significant charge transfer in the S_1 state; the $S_0 \rightarrow S_1$ transition involves mostly the central C3=C5 double-bond region, causing an elongation of this bond from 1.396 to 1.480 Å (S_0 *versus* S_1 keto minimum, CASSCF values). Other geometric parameters change only slightly (Fig. 1). According to single-point MS-CASPT2 calculations, S1-KETO lies 74.4 kcal mol^{-1} above S0-ENOL and 28.6 kcal mol^{-1} below S1-ENOL (Table 1). Thus, the excited-state proton transfer that yields the keto species is highly exothermic; in other words, 2-phenylphenol is a strong photoacid in S_1. As already mentioned, this proton transfer is computed to be essentially barrierless and is thus expected to be ultrafast. In terms of excited-state topology, our present results are consistent with recent RI-CC2 computations on a similar system, 2-phenyl-1-naphthol.[54]

Conical intersections

At the OM2/MRCI level, we were able to locate two S_1/S_0 minimum-energy conical intersections (S1S0-ENOL and S1S0-KETO). Selected bond lengths and dihedral angles are given in Fig. 1 and in Table 1, respectively. In S1S0-ENOL, the H10 atom is still attached to the O9 atom (phenol species) but the OH group is extruded out of the ring plane, with a C4C3C2O9 dihedral angle of −83° (OM2/MRCI). This strong out-of-plane deformation significantly increases the S_0 energy, thus closing the S_0–S_1 energy gap and reaching an S_1/S_0 conical intersection. In S1S0-KETO, the H10 atom is already bonded to the C7 atom (keto species); the two rings are not coplanar with a C2C3C5C7 dihedral angle of 58°. Energetically, S1S0-ENOL [S1S0-KETO] is computed to lie 92.1 [73.7] kcal mol^{-1} above the S0-ENOL ground state, and 21.4 kcal mol^{-1} [39.8 kcal mol^{-1}] below the S_1 energy at the Franck–Condon point (113.5 kcal mol^{-1}); hence, these two conical intersections are energetically accessible. Taking into consideration that S1S0-KETO is more stable than S1S0-ENOL by 18.4 kcal mol^{-1}, the former is expected to play a more vital role in excited-state deactivation.

It is worth stressing that OM2/MRCI and the *ab initio* methods give similar structures and energies for the two S_1/S_0 conical intersections (Table 1). Taking S1S0-ENOL as an example, the dihedral angles C2C3C5C7, C4C3C2O9, and C3C1C2O9 are computed to be −28°, −83°, and 141° at the OM2/MRCI level, compared with −35°, −97°, and 155° at the CASSCF level, respectively, (see Fig. 1). The relative energies from OM2/MRCI and single-point MS-CASPT2 calculations are also reasonably close to each other: the values of S1S0-ENOL [S1S0-KETO] are 92.1 [73.7] kcal mol^{-1} for OM2/MRCI, and 98.8/100.7 [69.8/73.9] kcal mol^{-1} for MS-CASPT2. In the latter case, the quoted S_0 and S_1 state energies differ slightly because they come from single-point MS-CASPT2 calculations at CASSCF-optimized geometries.

Excited-state decay paths

The preceding static electronic structure computations suggest the following scenario for the photoinduced processes in 2-phenylphenol. Upon irradiation, the spectroscopically bright S_1 state is populated in the Franck–Condon region, from which the S_1/S_0 conical intersection with an intact phenol moiety is energetically accessible (with relaxation to the ground state *via* S1S0-ENOL). A competitive process involves an essentially barrierless excited-state proton transfer yielding an S_1 keto minimum, which can decay to the ground state *via* the S_1/S_0 conical intersection in the keto region (S1S0-KETO); back in the S_0 state, the keto species S0-KETO can return to the more stable tautomer S0-ENOL *via* reverse ground-state hydrogen transfer.

To verify this mechanism and to explore the timescales of the underlying photophysical and photochemical events, we have performed trajectory-based fewest-switches surface-hopping dynamics simulations starting in the S_1 state of 2-phenylphenol.

Hopping-point distribution

The S_1–S_0 hopping-point distribution extracted from all surface-hopping trajectories reflects the topology of the conical intersection seam.[84] The two types of S_1/S_0 conical intersections in 2-phenylphenol, S1S0-ENOL and S1S0-KETO, clearly govern our nonadiabatic dynamics simulations. Fig. 4 depicts the distributions of the C7H10 distance and the C4C3C2O9 dihedral angle

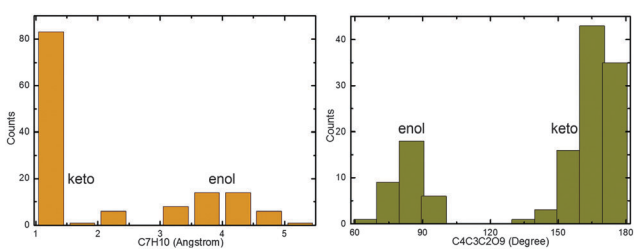

Fig. 4 Distribution of the C7H10 distance and the C4C3C2C9 dihedral angle at all S_1–S_0 hopping points. See text for detailed discussion.

at all S_1–S_0 hopping points. Obviously, there are two main hopping regions, which cluster around two minimum-energy S_1/S_0 conical intersections S1S0-ENOL and S1S0-KETO. A closer examination of the C7H10 distance distribution at all hopping points in Fig. 4 shows that most of the trajectories (67%) hop to the S_0 state *via* the keto conical intersection seam. This preference arises from two factors: first, the S_1 proton transfer is essentially barrierless so that the S_1 keto species is generated easily, and second, S1S0-KETO is thermodynamically favored over S1S0-ENOL because its potential energy is lower by 18.4 kcal mol^{-1} (OM2/MRCI). Hence, it is not surprising that most trajectories decay to the S_0 state *via* S1S0-KETO in our dynamics simulations.

S_1 lifetime

In our simulations, 118 of 148 (80%) trajectories have reached the S_0 state at the end of the 1 ps nonadiabatic dynamics runs. As shown in the left panel of Fig. 5, most of the $S_1 \rightarrow S_0$ hops happen between 100 and 400 fs (only 4 hops after 400 fs). Again, this ultrafast decay is consistent with the excited-state topological features, *i.e.* an almost barrierless proton transfer and two efficient deactivation channels (*vide supra*).

The S_1 excited-state deactivation can be viewed as a first-order elementary reaction. The S_1 state population is thus ruled by the following rate equation:

$$p(t) = \exp(-k(t - t_0)) + p_0 \quad (1)$$

where k is the corresponding rate constant; p_0 is the S_1 population at the end of the run (0.2 in this work); and t_0 is the initial delay time (57 fs). After fitting the time-dependent state population in Fig. 4 to eqn (1), we obtain an S_1 excited-state lifetime of 373 fs. One should note that the S_1 excited-state lifetime may be expected to increase in the condensed phase, in particular in a rigid environment.

Product distribution

Fig. 6 shows the product distribution at the end of the 1 ps nonadiabatic simulations. Overall, there are four kinds of products, namely S_1 enol (13%) and keto (5%), and S_0 enol (47%) and keto (35%); the enol : keto ratio is estimated to be 3 : 2. The top panel illustrates the distribution of the resulting phenol conformers. Most of the trajectories ending up in the phenol region have the H10 atom bonded to the O9 atom. However, there are also some S_0 phenol products that have the H8 atom bonded to the O9 atom, not the H10 atom (see H8O9 distribution). In these trajectories, the excited-state proton transfer and the reverse ground-state hydrogen transfer involve two different hydrogen atoms (H10 and H8, respectively). The bottom panel depicts the distribution of the keto conformers after the 1 ps simulations. There are *ca.* 90 trajectories with the H8 atom bonded to the C7 atom, and *ca.* 40 trajectories with the H10 atom bonded to the C7 atom.

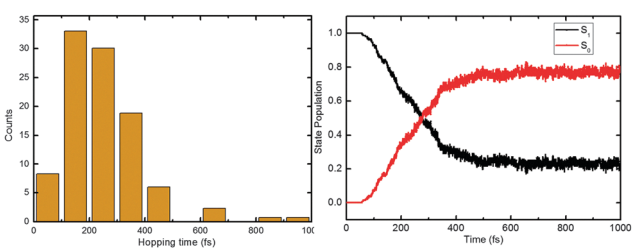

Fig. 5 Distribution of the S_1–S_0 hopping times (left) and time-dependent S_1 and S_0 state populations (right). See text for detailed discussion.

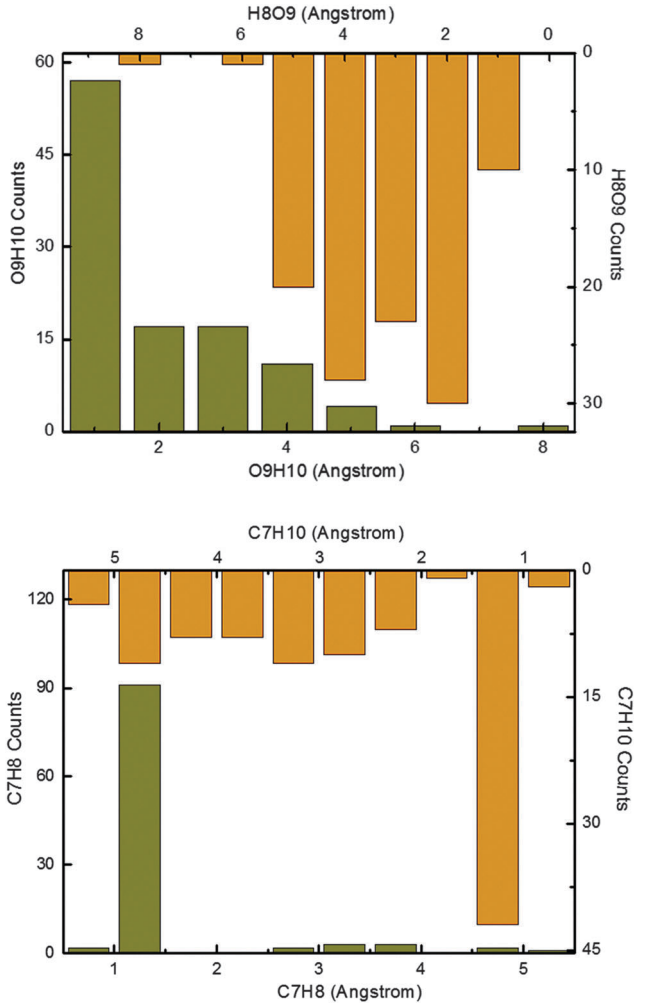

Fig. 6 Distribution of the C7H10, C7H8, H8O9, and O9H10 bond lengths at the end of 1 ps simulations. See text for detailed discussion.

Typical trajectories

In our nonadiabatic dynamics simulations, we see three different photocycles that start from S1-ENOL and end up at S0-ENOL: (I) the S_1 state decays directly to the ground state, without excited-state intramolecular proton transfer (ESIPT); (II) the S_1 state first evolves towards the S_1 keto species *via* an ultrafast barrierless ESIPT and then decays to the ground state in the keto region followed by a reverse ground-state hydrogen transfer (GSHT) involving the same migrating hydrogen atom; (III) the photocycle is the same as in case (II) except that different hydrogen atoms are involved in ESIPT and GSHT. In the following, we present for each

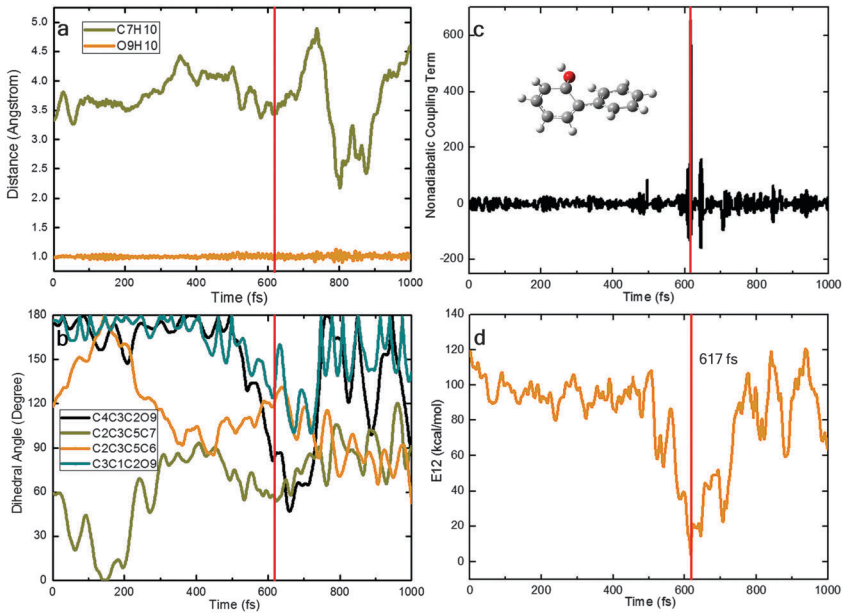

Fig. 7 Time-dependent physical variables obtained from a typical OM2/MRCI trajectory of type (I): (a) two key bond lengths; (b) four key dihedral angles; (c) nonadiabatic coupling term; and (d) S_1–S_0 energy gap.

photocycle pattern a representative trajectory to illustrate the main photophysical and photochemical events.

Fig. 7 shows a typical trajectory for case (I) with direct decay *via* the S1S0-ENOL conical intersection. Within the first 400 fs, the system starts to rotate around its central C3C5 bond (strong changes in the C2C3C5C6 and C2C3C5C7 dihedral angles; only small fluctuations in the C4C3C2O9 and C3C1C2O9 dihedral angles). During this process, the nonadiabatic coupling remains small and the S_1–S_0 energy gap remains large, so there is no nonadiabatic transition. After about 400 fs, the C4C3C2O9 dihedral angle starts to decrease from 180° to 40° at *ca.* 600 fs. The S_1 and S_0 states now become energetically close to each other (within 4 kcal mol^{-1}) and there is a large nonadiabatic coupling; thus, a nonadiabatic S_1–S_0 hop takes place, with relaxation of S_1 to the S_0 state. Thereafter, the C4C3C2O9 and C3C1C2O9 dihedral angles move back towards their original values (from twisted to a more planar arrangement). There is no ESIPT in this

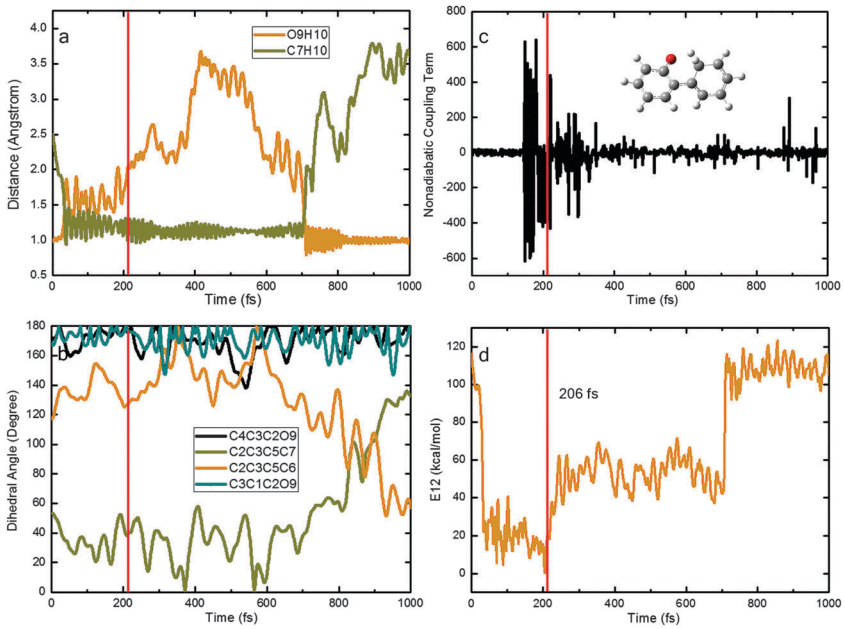

Fig. 8 Time-dependent physical variables obtained from a typical OM2/MRCI trajectory of type (II): (a) two key bond lengths; (b) four key dihedral angles; (c) nonadiabatic coupling term; and (d) S_1–S_0 energy gap.

trajectory. We emphasize that this photocycle pattern occurs only rarely in our trajectories.

Fig. 8 depicts a typical trajectory for case (II) with deactivation to the S_0 state *via* the S1S0-KETO conical intersection. In the initial stage of this trajectory, the O9H10 and C7H10 distances quickly increase and decrease, respectively. At *ca.* 50 fs, the ESIPT is complete and the S_1 keto species S1-KETO is formed, which remains in the S_1 state for another 150 fs (while retaining a rather short O9H10 distance indicative of excited-state hydrogen bonding interactions). Thereafter, it decays to the S_0 state at a point where the S_1–S_0 nonadiabatic coupling becomes very large (panel c) and the S_1–S_0 gap is very small (panel d). Interestingly, the generated S_0 keto species does not return back to the enol region immediately; instead, it roams the keto region for additional 500 fs. Then, a reverse ground-state hydrogen transfer takes place, regenerating the S_0 enol conformer and completing the photocycle. The rotation around the C3–C5 bond starts after *ca.* 700 fs (see the C2C3C5C6 and C2C3C5C7 dihedral angles in panel b) while the C4C3C2O9 and C3C1C2O9 dihedral angles do not vary much.

Fig. 9 presents a typical trajectory for case (III). Here, the O9H10 and C7H10 distances fluctuate around their equilibrium positions in the first 100 fs; then, they start to increase and decrease quickly. At about 110 fs, the S_1 keto species S1-KETO is formed, which stays in the S_1 state for *ca.* 50 fs and then decays to the S_0 state at 165 fs, when the keto S_1/S_0 conical intersection is encountered. The generated keto species roams the keto region in the S_0 state for a longer time (640 fs). After *ca.* 800 fs, the most stable S_0 phenol conformer is regenerated *via* a reverse ground-state hydrogen transfer. The rotation around the C3–C5 bond starts after *ca.* 900 fs (see the C2C3C5C6 and C2C3C5C7 dihedral angles in panel b). Interestingly, the H10 atom bonded to the O9 atom is transferred to the C7 atom in the ESIPT process, while the H8 atom originally bonded to the C7 atom is transferred to the O9 atom in the final GSHT step.

Discussion

Our results are consistent with the experiments available for 2-phenylphenol. Lukeman and Wan[49] argued that singlet reactivity is major for 2-phenylphenol, which is consistent with our computations. The S_1 excited-state proton transfer is nearly barrierless and ultrafast, so it is impossible for the system to efficiently populate triplet states in the Franck–Condon region. In addition, the $S_1 \rightarrow T_1$ intersystem crossing in the keto region is not expected to be competitive with the efficient internal conversion from the S_1 keto species to the S_0 state. However, this intersystem crossing could become more probable in a rigid environment because the internal conversion involves a large conformational change that could be impeded by steric interactions with the environment. Furthermore, there is experimental evidence that 2-phenylphenol is a strong photoacid in the S_1 state. This point is supported by the MS-CASPT2 results (see Fig. 10), which confirm that the S_1 excited-state proton transfer is highly exothermic – S1-KETO lies 28.6 kcal mol^{-1} below S1-ENOL and 40.6 kcal mol^{-1} below the initially populated S_1 Franck–Condon point.

We emphasize in this context that our present computations are carried out in vacuum and thus only consider the intrinsic photochemistry of 2-phenylphenol, for example, direct ESIPT processes to the *ortho*-position, without accounting for solvent-assisted intermolecular proton transfer to remote sites such as *para*-positions.

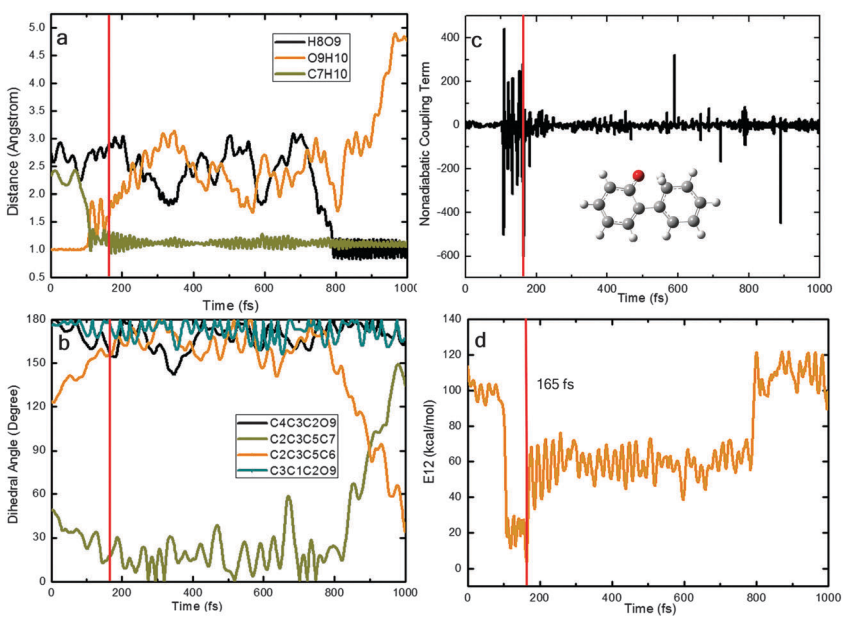

Fig. 9 Time-dependent physical variables obtained from a typical OM2/MRCI trajectory of type (III): (a) three key bond lengths; (b) four key dihedral angles; (c) nonadiabatic coupling term; and (d) S_1–S_0 energy gap.

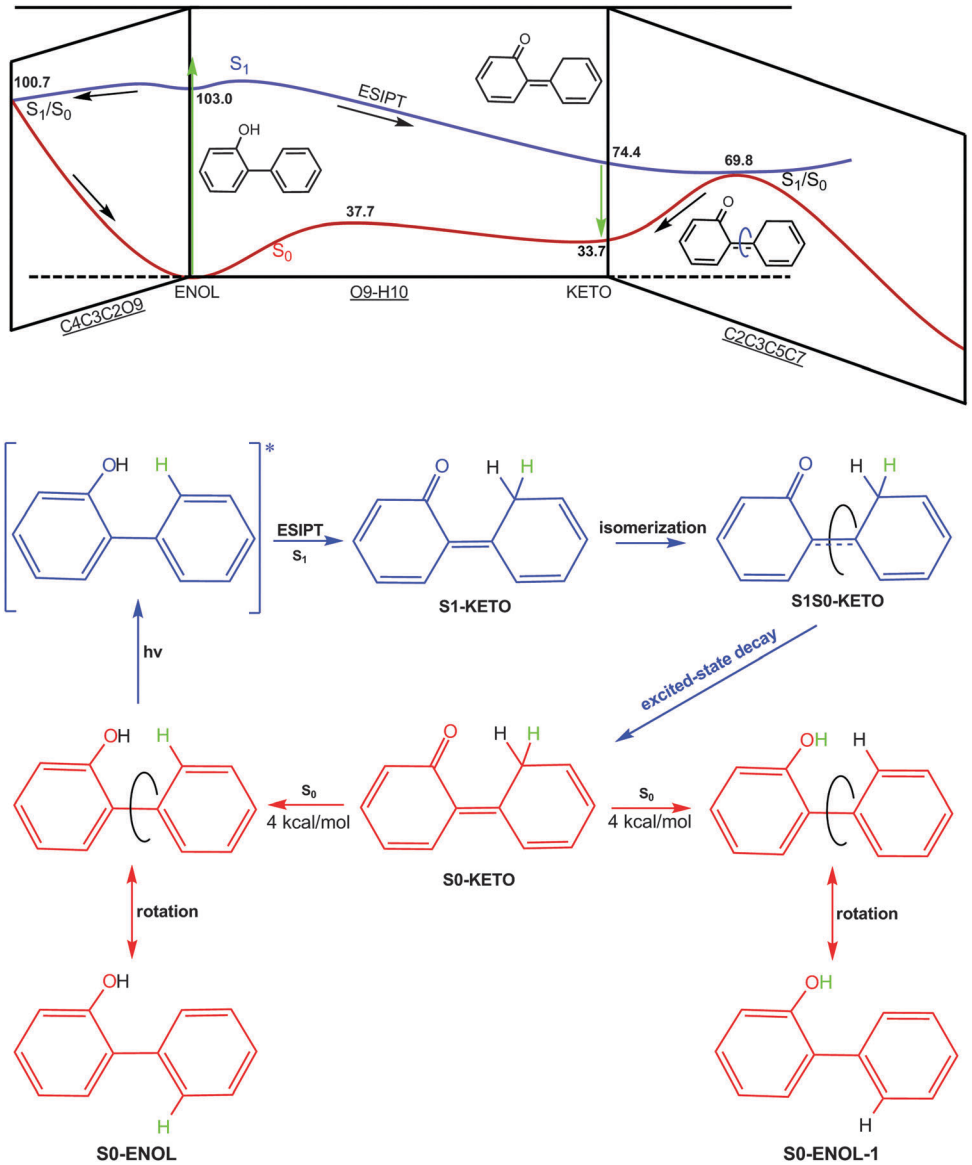

Fig. 10 S_1 deactivation pathways identified in the present work. Potential energy profiles and structures related to the S_0 and S_1 states are shown in red and blue, respectively. Also relative energies from single-point MS-CASPT2 computations (in kcal mol^{-1}) are given. See text for discussion.

Previous electronic structure computations on a similar system[54] showed that there exists an efficient S_1/S_0 conical intersection near the keto region, but without optimizing its structure. In this work we precisely located this kind of minimum-energy conical intersection in 2-phenylphenol, both at the OM2/MRCI and CASSCF levels (S1S0-KETO), and we explored its dynamical role in the S_1 photodynamics of 2-phenylphenol using full-dimensional surface-hopping dynamics simulations. We find that 67% trajectories decay to the S_0 state *via* this conical intersection in the keto region. In addition, we optimized the S_1/S_0 conical intersection in the Franck–Condon region (S1S0-ENOL), which also plays an important role in the S_1 deactivation (33%). Thus, both conical intersections need to be considered in order to correctly understand the mechanistic photochemistry of 2-phenylphenol and its variants.

How is the S_0 isomer S0-ENOL-1 (see the bottom of Fig. 10) generated in the photodynamics of 2-phenylphenol? Experimentally, Lukeman and Wan[49] assumed that this species comes from S0-KETO *via* a concerted reverse hydrogen transfer and 1,5-hydrogen shift. Our present dynamics simulations do not support this scenario – we do not see any 1,5-hydrogen shift in any of the trajectories. Instead, S0-ENOL-1 is generated by a simple single-bond rotation, after the hydrogen atom originally bonded to the phenyl ring has been transferred to the oxygen atom (Fig. 10).

The S_0 keto species has not yet been detected spectroscopically when using nanosecond laser flash photolysis.[49,54] B3LYP calculations indicate that the tautomerization of S0-KETO to the most stable phenol conformer S0-ENOL has to overcome a small barrier of 4.0 kcal mol^{-1}. It might thus be possible to observe this predicted transient species using ultrafast time-resolved transient spectroscopy.

Summary

With the use of electronic structure computations and trajectory-based surface-hopping dynamics simulations, we have for the first time explored the mechanistic photochemistry of 2-phenylphenol. We have simulated the S_1 excited-state proton transfer and deactivation as well as the reverse hydrogen transfer in the S_0 state. Mechanistically, some trajectories directly evolve from the Franck–Condon region toward an enol-type S_1/S_0 conical intersection, followed by an $S_1 \rightarrow S_0$ internal conversion to the ground-state minimum. Most of the trajectories proceed from the Franck–Condon region to the S_1 keto species *via* an essentially barrierless ESIPT; the transient S_1 keto species is then de-excited to the ground state *via* a second S_1/S_0 conical intersection in the keto region, followed by a quick relaxation back to the most stable phenol minimum *via* a reverse GSHT process (barrier of *ca.* 4 kcal mol^{-1} at the B3LYP level). The nonadiabatic dynamics simulations predict an average lifetime of 118 fs for the ESIPT process.[40,49] In these simulations, 67% of the trajectories decay to the S_0 state *via* the keto S_1/S_0 conical intersection, and 33% decay *via* the S_1/S_0 conical intersection in the Franck–Condon region. According to the computed time-dependent state populations, the S_1 excited-state lifetime is estimated to be 373 fs in vacuum. We hope that these computational results and mechanistic insights will stimulate further experimental work on 2-phenylphenol, especially by ultrafast time-resolved transient spectroscopy.

Acknowledgements

G.C. appreciates the financial support of ''The Recruitment Program of Global Youth Experts'' and ''Youth Scholars Program of Beijing Normal University''; W.T. is grateful for support from an ERC Advanced Grant.

References

1 E. Kosower and D. Huppert, *Annu. Rev. Phys. Chem.*, 1986, **37**, 127–156.
2 R. Mathies, S. Lin, J. Ames and W. Pollard, *Annu. Rev. Biophys. Biophys. Chem.*, 1991, **20**, 491–518.
3 R. Cukier and D. Nocera, *Annu. Rev. Phys. Chem.*, 1998, **49**, 337–369.
4 L. Tolbert and K. Solntsev, *Acc. Chem. Res.*, 2002, **35**, 19–27.
5 D. Stoner-Ma, A. Jaye, K. Ronayne, J. Nappa, S. Meech and P. Tonge, *J. Am. Chem. Soc.*, 2008, **130**, 1227–1235.
6 K. Choi and A. Hamilton, *Angew. Chem., Int. Ed.*, 2001, **40**, 3912–3915.
7 S. Kim, J. Seo, H. Jung, J.-J. Kim and S. Park, *Adv. Mater.*, 2005, **17**, 2077–2082.
8 S. Park, O.-H. Kwon, S. Kim, S. Park, M.-G. Choi, M. Cha, S. Park and D.-J. Jang, *J. Am. Chem. Soc.*, 2005, **127**, 10070–10074.
9 J. Kwon and S. Park, *Adv. Mater.*, 2011, **23**, 3615–3642.
10 A. Bard and M. Fox, *Acc. Chem. Res.*, 1995, **28**, 141–145.
11 D. Gust, T. Moore and A. Moore, *Acc. Chem. Res.*, 2001, **34**, 40–48.
12 W. Youngblood, S.-H. Lee, Y. Kobayashi, E. Hernandez-Pagan, P. Hoertz, T. Moore, A. Moore, D. Gust and T. Mallouk, *J. Am. Chem. Soc.*, 2009, **131**, 926–927.
13 R. Tsien, *Annu. Rev. Biochem.*, 1998, **67**, 509–544.
14 K.-Y. Chen, Y.-M. Cheng, C.-H. Lai, C.-C. Hsu, M.-L. Ho, G.-H. Lee and P.-T. Chou, *J. Am. Chem. Soc.*, 2007, **129**, 4534–4535.
15 S.-J. Lim, J. Seo and S. Park, *J. Am. Chem. Soc.*, 2006, **128**, 14542–14547.
16 W.-H. Fang, *J. Am. Chem. Soc.*, 1998, **120**, 7568–7576.
17 A. Sinicropi, R. Pogni, R. Basosi, M. Robb, G. Gramlich, W. Nau and M. Olivucci, *Angew. Chem., Int. Ed.*, 2001, **40**, 4185–4189.
18 A. Sobolewski, W. Domcke and C. Hättig, *Proc. Natl. Acad. Sci. U. S. A.*, 2005, **102**, 17903–17906.
19 J. Coe and T. Martínez, *J. Am. Chem. Soc.*, 2005, **127**, 4560–4561.
20 A. Sobolewski and W. Domcke, *J. Phys. Chem. A*, 2007, **111**, 11725–11735.
21 A. Migani, L. Blancafort, M. Robb and A. DeBellis, *J. Am. Chem. Soc.*, 2008, **130**, 6932–6933.
22 M. Barbatti, A. Aquino, H. Lischka, C. Schriever, S. Lochbrunner and E. Riedle, *Phys. Chem. Chem. Phys.*, 2009, **11**, 1406–1415.
23 F. Plasser, M. Barbatti, A. Aquino and H. Lischka, *J. Phys. Chem. A*, 2009, **113**, 8490–8499.
24 D. Shemesh, A. Sobolewski and W. Domcke, *J. Am. Chem. Soc.*, 2009, **131**, 1374–1375.
25 S. Olsen, K. Lamothe and T. Martínez, *J. Am. Chem. Soc.*, 2010, **132**, 1192–1193.
26 G. Cui, Z. Lan and W. Thiel, *J. Am. Chem. Soc.*, 2012, **134**, 1662–1672.
27 G. Cui and W. Thiel, *Phys. Chem. Chem. Phys.*, 2012, **14**, 12378–12384.
28 L. Spörkel, G. Cui, A. Koslowski and W. Thiel, *J. Phys. Chem. A*, 2013, **118**, 152–157.
29 L. Spörkel, G. Cui and W. Thiel, *J. Phys. Chem. A*, 2013, **117**, 4574–4583.
30 G. Cui, P.-J. Guan and W.-H. Fang, *J. Phys. Chem. A*, 2014, **118**, 4732–4739.
31 L. Serrano-Andrés and M. Merchán, *Chem. Phys. Lett.*, 2006, **418**, 569–575.
32 A. Kyrychenko and J. Waluk, *J. Phys. Chem. A*, 2006, **110**, 11958–11967.
33 H.-H. G. Tsai, H.-L. S. Sun and C.-J. Tan, *J. Phys. Chem. A*, 2010, **114**, 4065–4079.
34 G.-J. Zhao and K.-L. Han, *Acc. Chem. Res.*, 2012, **45**, 404–413.
35 Y. Shigemitsu, T. Mutai, H. Houjou and K. Araki, *J. Phys. Chem. A*, 2012, **116**, 12041–12048.
36 H. Fang and Y. Kim, *J. Chem. Theory Comput.*, 2013, **9**, 3557–3566.
37 Y. Houari, A. Charaf-Eddin, A. D. Laurent, J. Massue, R. Ziessel, G. Ulrich and D. Jacquemin, *Phys. Chem. Chem. Phys.*, 2014, **16**, 1319–1321.

38 M. Isaks, K. Yates and P. Kalanderopoulos, *J. Am. Chem. Soc.*, 1984, **106**, 2728–2730.
39 P. Kalanderopoulos and K. Yates, *J. Am. Chem. Soc.*, 1986, **108**, 6290–6295.
40 M. Lukeman and P. Wan, *Chem. Commun.*, 2001, 1004–1005.
41 P. Wan and G. Zhang, *Res. Chem. Intermed.*, 1993, **19**, 119–129.
42 N. Basarić and P. Wan, *Photochem. Photobiol. Sci.*, 2006, **5**, 656–664.
43 N. Aein and P. Wan, *J. Photochem. Photobiol., A*, 2009, **208**, 42–49.
44 N. Basarić, A. Franco-Cea, M. Alesković, K. Mlinarić-Majerski and P. Wan, *Photochem. Photobiol. Sci.*, 2010, **9**, 779–790.
45 Y.-H. Wang and P. Wan, *Photochem. Photobiol. Sci.*, 2011, **10**, 1934–1944.
46 N. Basarić, N. Doslić, J. Ivković, Y. H. Wang, J. Veljković, K. Mlinarić-Majerski and P. Wan, *J. Org. Chem.*, 2013, **78**, 1811–1823.
47 Y.-H. Wang and P. Wan, *Photochem. Photobiol. Sci.*, 2013, **12**, 1571–1588.
48 D. Skalamera, K. Mlinarić-Majerski, I. Martin-Kleiner, M. Kralj, P. Wan and N. Basarić, *J. Org. Chem.*, 2014, **79**, 4390–4397.
49 M. Lukeman and P. Wan, *J. Am. Chem. Soc.*, 2002, **124**, 9458–9464.
50 M. Lukeman and P. Wan, *J. Am. Chem. Soc.*, 2003, **125**, 1164–1165.
51 M. Flegel, M. Lukeman, L. Huck and P. Wan, *J. Am. Chem. Soc.*, 2004, **126**, 7890–7897.
52 N. Basarić and P. Wan, *J. Org. Chem.*, 2006, **71**, 2677–2686.
53 M. Nayak and P. Wan, *Photochem. Photobiol. Sci.*, 2008, **7**, 1544–1554.
54 N. Basarić, N. Doslić, J. Ivković, Y. H. Wang, M. Malis and P. Wan, *Chem. – Eur. J.*, 2012, **18**, 10617–10623.
55 S. Vosko, L. Wilk and M. Nusair, *Can. J. Phys.*, 1980, **58**, 1200–1211.
56 A. Becke, *Phys. Rev. A: At., Mol., Opt. Phys.*, 1988, **38**, 3098–3100.
57 C. Lee, W. Yang and R. Parr, *Phys. Rev. B: Condens. Matter Mater. Phys.*, 1988, **37**, 785–789.
58 A. Becke, *J. Chem. Phys.*, 1993, **98**, 1372–1377.
59 J. Schirmer, *Phys. Rev. A: At., Mol., Opt. Phys.*, 1982, **26**, 2395–2416.
60 A. Trofimov and J. Schirmer, *J. Phys. B: At., Mol. Opt. Phys.*, 1995, **28**, 2299–2324.
61 A. Köhn and C. Hättig, *J. Chem. Phys.*, 2003, **119**, 5021–5036.
62 C. Hättig, *Adv. Quantum Chem.*, 2005, **50**, 37–60.
63 A. Dreuw and M. Wormit, *Wiley Interdiscip. Rev.: Comput. Mol. Sci.*, 2015, **5**, 82–95.
64 K. Andersson, P. Malmqvist, B. Roos, A. Sadlej and K. Wolinski, *J. Phys. Chem.*, 1990, **94**, 5483–5488.
65 K. Andersson, P. Malmqvist and B. Roos, *J. Chem. Phys.*, 1992, **96**, 1218–1226.
66 N. Försberg and P. Malmqvist, *Chem. Phys. Lett.*, 1997, **274**, 196–204.
67 F. Aquilante, R. Lindh and T. Pedersen, *J. Chem. Phys.*, 2007, **127**, 114107–114713.
68 M. A. L. Marques, C. A. Ullrich, F. Nogueira, A. Rubio, K. Burke and E. K. U. Gross, *Time-dependent Density Functional Theory*, Springer, 2006.
69 T. Yanai, D. Tew and N. Handy, *Chem. Phys. Lett.*, 2004, **393**, 51–57.
70 R. Ditchfield, W. Hehre and J. Pople, *J. Chem. Phys.*, 1971, **54**, 724–728.
71 P. Hariharan and J. Pople, *Theor. Chem. Acc.*, 1973, **28**, 213–222.
72 A. Schäfer, H. Horn and R. Ahlrichs, *J. Chem. Phys.*, 1992, **97**, 2571–2577.
73 M. J. Frisch, G. W. Trucks, H. B. Schlegel, G. E. Scuseria, M. A. Robb, J. R. Cheesem, G. Scalmani, V. Barone, B. Mennucci, G. A. Petersson, H. Nakatsuji, M. Caricato, X. Li, H. P. Hratchian, A. F. Izmaylov, J. Bloino, G. Zheng, J. L. Sonnenberg, M. Hada, M. Ehara, K. Toyota, R. Fukuda, J. Hasegawa, M. Ishida, T. Nakajima, Y. Honda, O. Kitao, H. Nakai, T. Vreven, J. A. Montgomery Jr., J. E. Peralta, F. Ogliaro, M. Bearpark, J. J. Heyd, E. Brothers, K. N. Kudin, V. N. Staroverov, R. Kobayashi, J. Normand, K. Raghavachari, A. Rendell, J. C. Burant, S. S. Iyengar, J. Tomasi, M. Cossi, N. Rega, J. M. Millam, M. Klene, J. E. Knox, J. B. Cross, V. Bakken, C. Adamo, J. Jaramillo, R. Gomperts, R. E. Stratmann, O. Yazyev, A. J. Austin, R. Cammi, C. Pomelli, J. W. Ochterski, R. L. Martin, K. Morokuma, V. G. Zakrzewski, G. A. Voth, P. Salvador, J. J. Dannenberg, S. Dapprich, A. D. Daniels, O. Farkas, J. B. Foresman, J. V. Ortiz, J. Cioslowski and D. J. Fox, *Gaussian 09, Revision A.02*, Gaussian, Inc., Wallingford CT, 2009.
74 M. J. Frisch, G. W. Trucks, H. B. Schlegel, G. E. Scuseria, M. A. Robb, J. R. Cheeseman, J. A. Montgomery Jr., T. Vreven, K. N. Kudin, J. C. Burant, J. M. Millam, S. S. Iyengar, J. Tomasi, V. Barone, B. Mennucci, M. Cossi, G. Scalmani, N. Rega, G. A. Petersson, H. Nakatsuji, M. Hada, M. Ehara, K. Toyota, R. Fukuda, J. Hasegawa, M. Ishida, T. Nakajima, Y. Honda, O. Kitao, H. Nakai, M. Klene, X. Li, J. E. Knox, H. P. Hratchian, J. B. Cross, V. Bakken, C. Adamo, J. Jaramillo, R. Gomperts, R. E. Stratmann, O. Yazyev, A. J. Austin, R. Cammi, C. Pomelli, J. W. Ochterski, P. Y. Ayala, K. Morokuma, G. A. Voth, P. Salvador, J. J. Dannenberg, V. G. Zakrzewski, S. Dapprich, A. D. Daniels, M. C. Strain, O. Farkas, D. K. Malick, A. D. Rabuck, K. Raghavachari, J. B. Foresman, J. V. Ortiz, Q. Cui, A. G. Baboul, S. Clifford, J. Cioslowski, B. B. Stefanov, G. Liu, A. Liashenko, P. Piskorz, I. Komaromi, R. L. Martin, D. J. Fox, T. Keith, M. A. Al-Laham, C. Y. Peng, A. Nanayakkara, M. Challacombe, P. M. W. Gill, B. Johnson, W. Chen, M. W. Wong, C. Gonzalez and J. A. Pople, *Gaussian 03, Revision D.02*, Gaussian, Inc., Wallingford, CT, 2004.
75 F. Aquilante, L. De Vico, N. Ferré, G. Ghigo, P. Malmqvist, P. Neogrády, T. Pedersen, M. Pitonák, M. Reiher, B. Roos, L. Serrano-Andrés, M. Urban, V. Veryazov and R. Lindh, *J. Comput. Chem.*, 2010, **31**, 224–247.

76 TURBOMOLE V6.5 2013, a development of University of Karlsruhe andForschungszentrum Karlsruhe GmbH, 1989-2007, TURBOMOLE GmbH, since 2007; available from http://www.turbomole.com.
77 W. Weber, PhD thesis, University of Zürich, 1996.
78 W. Weber and W. Thiel, *Theor. Chem. Acc.*, 2000, **103**, 495–506.
79 A. Koslowski, M. E. Beck and W. Thiel, *J. Comput. Chem.*, 2003, **24**, 714–726.
80 W. Thiel, *MNDO99 program, version 6.1*, Max-Planck-Institut für Kohlenforschung, Mülheim, Germany, 2007.
81 D. Yarkony, *J. Chem. Phys.*, 2001, **114**, 2601–2613.
82 T. W. Keal, A. Koslowski and W. Thiel, *Theor. Chem. Acc.*, 2007, **118**, 837–844.
83 G. Granucci, M. Persico and A. Zoccante, *J. Chem. Phys.*, 2010, **133**, 134111–134119.
84 G. Cui and W. Thiel, *Angew. Chem., Int. Ed.*, 2013, **52**, 433–436.
85 O. Weingart, Z. Lan, A. Koslowski and W. Thiel, *J. Phys. Chem. Lett.*, 2011, **2**, 1506–1509.
86 A. Kazaryan, Z. Lan, L. Schäfer, W. Thiel and M. Filatov, *J. Chem. Theory Comput.*, 2011, **7**, 2189–2199.